

# Automated Processing to derive Dip Angles of Englacial Radar Reflectors in Ice Sheets

Louise C. Sime<sup>1\*</sup>, Richard. C. A. Hindmarsh<sup>1</sup>, and Hugh. Corr<sup>1</sup>

<sup>1</sup>*British Antarctic Survey, Cambridge, CB3 0ET, U.K.*

*E-mail: lsim@bas.ac.uk*

**ABSTRACT.** We present a novel automated processing method for obtaining layer dip from radio-echo sounding (RES) data. The method is robust, easily applicable, and can be used to process large (several terabyte) ground and airborne RES datasets using modest computing resources. Test results are presented from applying the method to two Antarctic datasets: the Fletcher Promontory ground-based radar dataset and the Wilkes Subglacial Basin airborne radar dataset. The automated RES processing (ARESP) method comprises six basic steps: (1) RES noise reduction; (2) radar layer identification; (3) isolation of individual ‘layer objects’; (4) measurement of orientation and other object properties; (5) elimination of noise in the orientation data; and (6) collation of the valid dip information. Resultant apparent dip datasets produced by the method will aid glaciologists seeking to understand ice flow dynamics in Greenland and Antarctica: ARESP could enable a shift from selective regional case studies to ice-sheet scale studies.

## INTRODUCTION

The IPCC Fourth Assessment Report notes that there is considerable uncertainty associated with projected sea level change over the coming decades and century (IPCC, 2007). Understanding ice flow dynamics in Greenland and Antarctica is an urgent climate problem; even a modest change in ice sheet volume will strongly affect future sea level and freshwater flux to the oceans (Lemke and others, 2007). However past, present, and future ice flow, both by internal deformation and basal sliding, is poorly understood. This uncertainty could be substantially reduced by more and better use of observations of the internal structure of the Greenland and Antarctic ice-sheets.

25 Internal layering is frequently observed in radio-echo soundings (RES) of ice-sheets, as well as in smaller polar glaciers. Most  
26 internal ice reflectors in these datasets are thought to be isochronous (Bogorodsky and others, 1985). For this reason, the RES  
27 architecture provides a picture of the age structure of the ice (Eisen, 2008). RES data from both ground and airborne based  
28 instruments have therefore been used: to investigate changes in ice flow (*e.g.* Siegert and others, 2004; Rippin and others,  
29 2006); in ice flow modelling studies (Conway and others, 1999; Siegert and others, 2003; Martín and others, 2006; Waddington  
30 and others, 2007; Eisen, 2008; Martín and others, 2009); to calculate past accumulation rates (Fahnestock and others, 2001);  
31 and for the constraint of layer ages from ice cores (Waddington and others, 2007).

32 Gathering of isochronous layer information from RES data has traditionally been done by picking out and following individual  
33 reflectors within RES datasets (*e.g.* Nereson and others, 2000; Nereson and Raymond, 2001; Waddington and others, 2007).  
34 This approach requires reflectors with excellent continuity that can be traced for long distances. One application is to use  
35 these data in conjunction with ice-flow models that predict isochrones to directly compare model results with tracked layer  
36 observations.

37 A primary consideration in obtaining layer information from RES data is amount of labour required to carry out the data  
38 gathering. We can use hand-picking of bed profiles (*e.g.* Lythe and others, 2001) to calculate how much effort is required  
39 to manually pick ice reflectors in RES sections. Since 20 000 km of the WISE-ISODYN survey took six months of work to  
40 hand-pick the bed with a skilled operative, this suggests that picking twenty internal ice reflectors would take about ten  
41 years of work. Thus, while hand-picked continuous isochrones can provide an excellent product, hand-picking of internal ice  
42 reflectors at all depths along new extensive RES datasets (these are now available across hundreds of thousands of kilometers  
43 of flight line) is prohibitive in terms of required man-hours. While some largely automated layer-picking techniques have been  
44 developed (*e.g.* Fahnestock and others, 2001; Matsuoka and others, 2009), these still require some operator input.

45 A second consideration in obtaining layer information is the dependency on continuity. Manual and auto-picking methods  
46 are both restricted in applicability to RES datasets with very good reflector continuity. However, Parrenin and others (2006)  
47 and Parrenin and Hindmarsh (2007) note that identical flow information is contained in the apparent dip of the reflectors. This  
48 is useful because dip datasets can be derived from localised reflector information without requiring long-distance continuity.  
49 (Note, for brevity we generally use the term ‘dip’ to refer to the ‘apparent dip’ of the isochrones, and if needed, refer to  
50 the maximum dip, which is generally not orientated parallel to a survey line, as the true dip. Throughout this paper dip  
51 refers strictly to the tangent of the observed RES reflector slope at a given point. ). A constructive proof of the isochrone-dip  
52 equivalence is given in Parrenin and others (2006), who derive an explicit formula for the evolution of dip along a streamline.  
53 A more intuitive way to recognize this is to note that isochrones contain no information about horizontal provenance, and are

54 consequently just geometric features that can be equally characterized by their dip. The corollary of this is that continuous  
55 apparent dips can also be integrated to provide synthetic isochrones.

56 Note that, in practice, we require reflector segments of a finite length to measure dip, and this means that the measured dip  
57 is not strictly a point measurement. However, by comparison with forward numerical ice flow models, the spatial averaging of  
58 the observed dip datasets generated here is smaller than spatial averaging using typical numerical model grid resolutions. This  
59 implies that, in most circumstances, individually hand-picked reflectors or continuous sections of apparent dip can equally well  
60 be used.

61 Since ice flow models calculate age as a field that depends upon horizontal and vertical position (*e.g.* Hindmarsh and  
62 others, 2009) the modelled slope of the age field at a given elevation in a given horizontal direction can be compared with dip  
63 observations. In other words, we can compare observed and modelled dips directly rather than reconstitute observed dips into  
64 isochrones to compare with isochrones outputted from models. Because the measured dips are quantitative data, possibilities  
65 of using these data within inverse frameworks also arise. For direct model-observational comparison or for inverse modelling,  
66 there is an issue of how the quantity of observational data will affect the study, and hence how much dip data may need to  
67 be retrieved, which we do not address in this paper. However we note that because the emphasis on continuity of reflectors is  
68 substantially reduced by our approach, and the manual effort required is very small, this increases substantially the quantity  
69 of useable datasets.

70 Most glaciologists would argue that good continuous reflectors are better than angle information. By the Fundamental  
71 Theorem of Calculus, the two are mathematically equivalent; a dip field can be integrated to give isochrones. In practical  
72 terms, very continuous reflectors are associated with very high quality data, and there is very little difference in practice  
73 between automatic picking (which uses the local slope as a predictor) and our method. Although our method also works where  
74 there is poor continuity, in other words where data quality is worse, our results will also be worse. Of course, with very high  
75 quality data, more data analysis options are available, for example stratigraphic correlation, and at this point one has to start  
76 considering how precisely radar reflectors map onto isochrones.

77 Here, we present the novel automated finite segment method to obtain englacial reflector dip angles from either airborne  
78 or ground-based RES data. We emphasize that the automated RES processing (ARESP) method is based on measuring local  
79 dip: ARESP is not an auto-picking routine, and does not rely on internal reflectors remaining traceable over whole section.  
80 However, the dip datasets produced by ARESP are horizontally integrated here to provide synthetic isochrones, since these  
81 are useful to help assess the quality of ARESP dip data. But despite this appearing similar to a tracked-layer method, these  
82 results are produced using an approach quite distinct from an automated version of a tracked-layer method.

83 To test the ARESP method we apply it to two specific RES datasets which appear to be fairly typical of recent ground-based  
84 and airborne RES. Firstly the 22 km Fletcher Promontory radar line, surveyed using the ground-based DELORES radar, and  
85 secondly the 1007 km Wilkes Subglacial Basin airborne RES line (Table 1 for RES dataset characteristics).

## 86 **SAMPLE DATA**

87 RES systems operate by emitting a radar pulse which propagates through the air and the ice sheet. Energy from the pulse is  
88 reflected at boundaries between materials of differing dielectric properties and the return signal is recorded. More details can  
89 be found in Bogorodsky and others (1985).

90 RES surveys can take place from the air or from the ground. Airborne systems do not always provide the same reflector  
91 continuity as the lower frequency, higher resolution ground-based systems. The choice of which system to use is severely  
92 constrained by logistical considerations as well as the scientific scope of the surveying. Here we demonstrate that, for a  
93 tractable ground-based RES dataset, ARESP dips are as good as those derived from hand-picking ice reflectors. For a less  
94 pickable airborne dataset, ARESP also performs convincingly.

### 95 **Example ground-based data: The Fletcher Promontory**

96 During December 2005 the Fletcher Promontory in West Antarctica was surveyed using the BAS ground-based DELORES  
97 radar at 100 MHz, with an effective band width after processing of 5 MHz, and a a nominal centre-frequency of 7 MHz  
98 (Hindmarsh and others, submitted), see Table 1. A trace of 900 returning pulses (sampled at 100 MHz), allow depiction of  
99 the full depth of the 600 m thick ice. This dataset has undergone some initial trace stacking and horizontal smoothing prior  
100 to the application of our ARESP method. The average resultant horizontal trace resolution is 2.73 m. Figure 1a shows a  
101 sample portion of the 22 km Fletcher dataset. For simplicity we present the Figure 1a RES dataset as localised standard  
102 scores, where the standard score is a dimensionless quantity derived by subtracting the local RES dataset population mean  
103 from an individual raw score and then dividing the difference by the local population standard deviation. The size of the local  
104 population for this conversion spans approximately two ice reflectors in the vertical. (Note, we convert the data only to provide  
105 an initial depiction of the dataset: the Processing Method described hereafter is applied to the raw unconverted data.)

### 106 **Example airborne data: The Wilkes Subglacial Basin**

107 During the austral summer of 2005 and 2006 a collaborative UK-Italian project (WISE-ISODYN) conducted an extensive  
108 airborne geophysical survey of the Transantarctic Mountains, Wilkes Subglacial Basin and the Dome C region (Ferraccioli and  
109 others, 2007). We use a 1007 km long flight line from this dataset (for brevity, hereafter referred to as the WSB data).

110 For the WSB data (Table 1), a trace of 1400 returns are sampled at 22 MHz, with an effective band width after processing  
111 of 5 MHz, and a a nominal centre-frequency of 150 MHz (Corr and others, 2007). Twenty five of these samples are stacked to

112 record the trace returns at 312.5 Hz, or roughly every 0.2 m, at the given WSB flight-speed, along the flight path. This yields  
 113 a total recorded WSB dataset size of 47 GB. During the initial recording and pre-processing stage the received pulses are fed  
 114 through a high gain chirp channel where the chirp is compressed. This airborne example, unlike the ground-based example  
 115 above, has therefore not had any initial pre-processing applied, apart from the stacking and onboard processing that occurs  
 116 during the initial echo recording.

117 Figure 1b shows a 59.63 km sample section of the total 1007 km long WSB dataset: the sample section starts at  $72.85^\circ$  S  
 118  $159.04^\circ$  E and ends at  $73.03^\circ$  S  $157.31^\circ$  E and is formed of approximately 300 000 traces, or about 7% of the total 47 GB  
 119 WSB dataset, with a horizontal trace separation ( $\Delta x_1$ ) of about 0.2 m. Note the data shown has been converted to localized  
 120 standard scores to enable this initial visualization of the reflectors (it does not represent ‘raw’ data). The WSB ice thickness  
 121 in the first 60 km of section varies between about 2.1 and 3.3 km. Figure 1b therefore shows the echo returns recorded down  
 122 to  $42 \mu\text{s}$ , or about 3.5 km, in depth (as standard scores). Reflectors can be detected throughout most of the dataset, with the  
 123 exception of the upper few hundred metres, and the few hundred metres closest to the bed.

## 124 PROCESSING METHOD

125 Here, we outline the fully automated processing method (Figure 2) which we apply to the initial echo return strength datasets  
 126 (herein these RES datasets are referred to as  $P$ ). In summary the steps are: (1) reduce RES inter-trace noise by horizontal  
 127 averaging; (2) obtain binary dataset by local thresholding; (3) identify short coherent layer segments, or ‘layer objects’, by  
 128 horizontal discretization of the binary data; (4) measure layer object properties; (5) discard invalid layer objects; and (6)  
 129 collate the non-uniformly distributed object dip information. Note we use layers here to refer here to reflectors with a finite  
 130 thickness. See Table 2 for the two dimensional arrays used during the processing, and Table 3 for RES data properties and  
 131 ARES parameters used.

### 132 Step 1: Noise reduction

133 Initial processing is designed simply to reduce inter-trace noise. Adjacent traces ( $\Delta x_1 = 0.2$  m apart) in the  $P^{WSB}$  can  
 134 feature echo amplitudes which are an order of magnitude different. The correlation between the adjacent traces is also quite  
 135 low (typically  $R = 0.80$  for traces around 5 m apart). Since the RES ice layers tend to show a strong degree of horizontal  
 136 persistence, it is possible to enhance the signal to noise ratio by simple horizontal averaging.

137 Firstly, a moving average of length scale  $L_x = 500$  adjacent traces at a time (approximately 100 m of radar section) is  
 138 performed to increase the signal to noise ratio. Initial investigations of the RES data (during trial runs of ARES) indicate  
 139 that layer slopes do not tend to exceed 30% in our test datasets. Therefore averaging 50 m on either side ensures that generally  
 140 we are averaging within, rather than through, dipping layers. This yields long lengths of continuous radar layer. Secondly, the

141 horizontal resolution is reduced by a factor of ten, to account for the subsequent ‘oversampling’ induced by the horizontal  
 142 averaging, to leave a horizontal resolution  $\Delta x_2 = 2$  m, *i.e.* one trace every 2 m. This stage produces an initial horizontally  
 143 averaged ‘noise reduced’ version of  $P$  which we term  $\overline{P_x}$ . The horizontal pixel length ( $\Delta x_2$ ) of 2 m also roughly corresponds  
 144 to the average trace distance of 2.73 m for the Fletcher RES dataset.

145 Additionally, a version of  $P$  with vertical averaging, to further reduce noise, is calculated. This is done by applying a vertical  
 146 moving mean, with a length scale of half of a typical vertical layer wavelength (*i.e.* averaging length scale  $L_{z1} = 0.5 \times \lambda$ ), to  
 147  $\overline{P_x}$  to produce  $\overline{P_{xz1}}$ . This yields an array the same size as  $\overline{P_x}$ , in which layers which are less than about 38 m for WSB, and 8  
 148 m for Fletcher, thick are smoothed out.

149 Note, because the ground-based example RES dataset had undergone horizontal averaging prior to our obtaining the dataset,  
 150 we do not need to apply this initial horizontal averaging ‘noise reduction’ step to obtain  $\overline{P_x}$  for the Fletcher Promontory data:  
 151  $\overline{P_x}$  is effectively the  $P^{Fletcher}$  initial dataset. However all other steps, including the second noise reduction stage (to obtain  
 152  $\overline{P_{xz1}}$ ), are applied identically to obtain both our ground-based and airborne test RES datasets.

## 153 **Step 2: Obtaining a Binary Layer Dataset**

### 154 *Approaches to thresholding*

155 There are two main approaches to identifying layer boundaries using noise reduced  $P$ : either simply thresholding the original  
 156 data, or thresholding a first- or second-derivative product obtained by filtering. During the thresholding process, individual  
 157 RES values are marked as ‘layer’ pixels if their value is greater than the defined threshold value (assuming a layer to be higher  
 158 value than the local background) and otherwise as ‘not layer’ pixels. The simple thresholding works on the assumption that  
 159 layers with low returns represent gaps between more reflective layers. The other approach, of thresholding dataset derivatives,  
 160 works on the assumption that the zones of most rapid change in intensity occur between layers. Sophisticated second-derivative  
 161 methods such as the Canny approach (Canny, 1986), take this a stage further and compute the local maximum of the gradient  
 162 of image intensity. These derivative methods can have the advantage of defining edges only a single value deep and/or wide,  
 163 so it may be the best option in situations with strong layer edge definition, but it can be sensitive to noise (*e.g.* Sime and  
 164 Ferguson, 2003).

165 Initial tests (not shown) suggest that first and second-derivative products are rather sensitive to RES noise, and are unreliable  
 166 for airborne RES data, even after our noise reduction processing (Step 1). As such, they not explored further here, but it may  
 167 be of interest to examine derivative methods further when considering possible future radar layer processing developments.  
 168 Instead, a robust means to automatically find layers, is through the production of binary ‘layer or not layer’ data by directly  
 169 thresholding the  $\overline{P_x}$  and  $\overline{P_{xz1}}$  arrays.

### 170 *Thresholding using a localised threshold*

171 The noise reduced  $\overline{P_x}$  and  $\overline{P_{xz1}}$  arrays still have regional contrasts in intensity, and a large reduction in echo strength with  
 172 depth. A localised threshold value helps to correct for these regional differences. A threshold array, the same size as the noise  
 173 reduced data array, is calculated. This is done by applying a longer length scale vertical moving mean. The length scale used  
 174 is twice the typical vertical layer wavelength (*i.e.* averaging length scale  $L_{z2} = 2 \times \lambda$ ), to  $\overline{P_x}$  to obtain  $\overline{P_{xz2}}$ . The array  $\overline{P_{xz2}}$   
 175 has all individual reflectors smoothed out, but it retains regional changes (*i.e.* over tens to hundreds of metres) in  $P$ .

176 Binary datasets are obtained by subtracting the threshold array  $\overline{P_{xz2}}$  from  $\overline{P_x}$  and  $\overline{P_{xz1}}$  and retaining the sign of the  
 177 resultant array, *i.e.* the binary dataset  $B_1 = \text{sign}(\overline{P_x} - \overline{P_{xz2}})$  and a second binary dataset, with reduced intra-layer noise,  
 178  $B_2 = \text{sign}(\overline{P_{xz1}} - \overline{P_{xz2}})$ . Note *sign* means any value above zero is classified as ‘layer’, any value below zero is classified as  
 179 ‘not layer’ (*e.g.* see Figure 2c). By definition, thresholding using  $\overline{P_{xz2}}$  ensures that the binary datasets  $B_1$  and  $B_2$  are both  
 180 approximately 50% of reflective ‘layer’ (logically positive), and 50% unreflective ‘not layer’ (logically negative).

181 Whilst using the two separate  $B_1$  and  $B_2$  arrays is not essential, it does provide a more robust characterization of layer  
 182 dips, because the arrays identify layers of different thicknesses. For some regions  $B_1$  reliably identifies thinner layers, whilst  
 183 for other noisy regions  $B_2$  provides more reliable identification for thicker layers. Note, throughout the subsequent steps 3 to  
 184 5 the binary layer datasets  $B_1$  and  $B_2$  are processed separately. Then all the dips measured from both  $B_1$  and  $B_2$  are collated  
 185 during step 6 to provide a thorough survey of the radar layer angles.

### 186 **Step 3. Obtaining Layer Dips**

187 Calculating the binary datasets  $B_1$  and  $B_2$ , while bringing out the ice layers, does not quantify the dip angle information. We  
 188 still need to measure these dip values.

#### 190 *Step 3a: Isolating ‘layer objects’*

191 The next stage of the automated processing is to extract dip information. This stage is begun by horizontally separating the  
 192 binary arrays into thin vertical strips. ‘Layer objects’ are isolated by using a horizontal separation length  $S_1$  of 25 horizontal  
 193 pixel (or roughly 50 m) for  $B_1$  and a separation length  $S_2$  of 50 pixels (roughly 100 m), for the two binary arrays (*e.g.* Figure  
 194 2d). An ‘object’ in this sense is a selection of values adjacent to each other, within the same strip, which are all of the same  
 195 logical value *i.e.* which comprise a short horizontal strip of identifiable radar layer. The binary arrays are also inverted so  
 196 that ‘layer objects’ are identified also using the low, as well as high, reflectivity as a criteria (not illustrated in Figure 2). To  
 197 maximize the number of ‘layer objects’ identified,  $B_1$  and  $B_2$  can also be sampled in overlapping strips.

198 *Step 3b: Measuring ‘layer objects’*

199 Once ‘layer objects’ are identified (as individual selections of adjacent values with the same logical property), by horizontally  
 200 separating the objects in discrete strips (Step 3a), the properties of the individual objects are measured. Morphological  
 201 measurements are made of the object position, area, major axis length, minor axis length, and orientation (Figure 2e). Object  
 202 area, major axis length, and minor axis length are used to assess whether the object is likely to give accurate layer orientation  
 203 information *i.e.* is a valid ‘layer object’ or ‘noise’, whilst object position is needed to locate each valid layer object.

204 *Step 3c: Eliminating invalid ‘layer objects’*

205 Several criteria are used to find layer ‘noise’ *i.e.* measured objects which would provide erroneous layer dip data (see also Table  
 206 3). Firstly, any object which is too small to be reliable as a layer object is removed from the analysis. The pixel area  $A_1$  is used  
 207 as the criteria for removal; some examples can be seen in Figure 2e. Secondly, any object with an area which is too large, where  
 208 it may comprise several ‘true’ layers, is likely to provide inaccurate dip information. Here, the pixel area  $A_2$  is used as the  
 209 criteria for removal. Thirdly, any object possessing a pixel aspect ratio  $r$  of less than three to one is eliminated: approximately  
 210 equi-axial objects do not provide reliable dip estimates. The remainder of the layer object information is retained.

211 *Step 3d: Collating ‘layer object’ angle data*

212 Finally, the object dip information is collated by location. The automatically measured ‘layer objects’ are not distributed  
 213 uniformly across the radar section. A gridded dip dataset is formed by taking the median of local sets of dip estimates (gridded  
 214 results are shown in Figure 3a and 4a). Tests (not shown) indicate that the sample size used for this gridding procedure  
 215 does not have a strong impact on these results, provided the number is kept high enough to provide a statistically robust  
 216 sample (for our sample datasets this is around 80). Note that Figure 2d and 2e illustrates dip measurements being made  
 217 on a horizontally compressed version of the binary data. The example section shown in Figure 2de is roughly 4 km long, so  
 218 the ARES processing method in reality samples roughly 1200 objects per layer across this section of data, rather than the  
 219 illustrative four objects per layer shown in Figure 2d.

220 **Results**

221 Example sections from the ground-based Fletcher Promontory and WSB airborne RES datasets are shown in Figure 3 and 4,  
 222 respectively. Upper panels illustrate the collated gridded ARES ice layer dip data, whilst lowest panels show some ‘synthetic  
 223 isochrones’ projected from the ARES dip data, over binary  $B_2$  arrays. For the ground-based Fletcher dataset, visual inspection  
 224 of Figure 3b indicates that ARES results are as good as those which would be obtained from hand-picking layers.

225 The large set of automatically detected and measured ‘layer objects’ enables errors associated with the automatic detection  
 226 method, and with RES data noise, to be quantified. For example, Figure 4b shows the standard deviation associated with

227 local sets of dip observations. High values show that the ‘layer objects’ measured are quite variable in dip; the collated ‘layer  
228 object’ dip data (Figure 4a) is uncertain in these regions. The near surface and near bed regions stand out as having uncertain  
229 ice layer dips.

230 Inspection of Figure 4c suggests that some RES reflectors in the airborne dataset may be discontinuous. The standard  
231 deviation (Figure 4b) confirms that whilst reflectors can be detected throughout most of the dataset, the upper few hundred  
232 metres and the few hundred metres closest to the bed, do not have reliably detectable coherent ice reflectors. Additionally,  
233 some high angle radar artifact layers are visible in near bed regions associated with high bed dips (within the first 20 km of  
234 the flight line). Together these cause a near bed region, at about 24-33  $\mu S$  in depth and 4-12 km track distance, where the ice  
235 reflector dips cannot be accurately ascertained (red region above the bed in Figure 4b). In consequence, we do not attempt  
236 to project layers (synthetic isochrones) over this region, since ARESF cannot provide reliable dip angles in this region. For  
237 regions where RES ice reflectors are more coherent, the Figure 4c airborne RES projected line results are comparable to those  
238 which would be obtained from hand-picking methods.

## 239 CONCLUSION

240 The novel automated method presented here is robust: identical ARESF using identical parameter values function equally  
241 well on recent airborne and ground-based RES datasets, without the need for any ARESF parameter tuning. Additional tests  
242 indicate that ARESF, as presented here, also performs equally well on alternative ground-based and airborne datasets (not  
243 shown). However, we note that minor changes in the ARESF parameter values, such as in the noise reduction ( $L_x$  and  $L_z$   
244 averaging lengths), and the criteria used to eliminate invalid ‘layer objects’ (*i.e.*  $A_1$  and  $A_2$ ), are likely to be required to  
245 optimise ARESF for differing RES datasets. Automating the specification of  $\lambda$ , and setting the ARESF parameters to be  
246 functions of  $\lambda$ , may enable future ARESF developments to minimise any dataset specific parameterisation changes.

247 In terms of processing time required, on a modest desktop computer (3 GHz clock speed, with 3 GB RAM), the WSB  
248 dataset (1007 km in length, and 47 GB in size) were processed in around 10 wall-clock hours and the 22 km Fletcher example  
249 took a few minutes. This implies that on this setup, 1 TB (or around 20 000 km) of airborne data can be processed in less than  
250 a week. Setting up the ARESF algorithms on a high performance multi-processor environment, and/or using higher speed  
251 disks, could enable faster processing of RES data.

252 While hand-picked continuous isochrones are a very good product, hand-picking large RES datasets for lots of ice reflectors  
253 is not generally feasible in terms of manual effort required: applying ARESF to the  $> 100\,000$  km of airborne line surveys of  
254 East Antarctica, can potentially save more than half a century of manual labour.

255 As well as the time saving advantage, the ARESF method has other possible advantages over the manual hand-picking  
256 method. Firstly, because ARESF uses only local reflector dip information, continuous reflectors along the whole length of the

257 RES section are not necessary to allow collation of ARESP dip datasets. Secondly, the relatively complete ARESP measurement  
258 of local ice reflector dips can allow a thorough characterisation of dip angle uncertainty. These advantages may allow ARESP  
259 to help with ice-flow model-data comparison studies and with inverse model studies.

260 In conclusion, the efficiently processed dip angle datasets produced by the ARESP method should substantially help glaciol-  
261 ogists seeking to understand ice flow dynamics in Greenland and Antarctica. ARESP has the potential to change the way we  
262 model isochrones: it could enable glaciologists to move from selective case studies to large-scale studies using all available RES  
263 ice reflector data.

## 264 **ACKNOWLEDGEMENTS**

265 The authors thank Kenny Matsuoka and an anonymous reviewer for helpful comments which improved the manuscript. This  
266 study is part of the British Antarctic Survey Polar Science for Planet Earth Programme. It was funded by The Natural  
267 Environment Research Council.

## 268 **REFERENCES**

- 269 Bogorodsky, V. V., C. R. Bentley and P. E. Gudmandsen, 1985. Radioglaciology (Glaciology and Quaternary Geology), Springer.
- 270 Canny, J, 1986. A computational approach to edge detection, IEEE Trans. Pattern Anal. Mach. Intell., **8**(6), 679–698.
- 271 Conway, H., B. L. Hall, G. H. Denton, A. M. Gades and E. D. Waddington, 1999. Past and future grounding-line retreat of the West  
272 Antarctic Ice Sheet, Science, **286**, 280–283.
- 273 Corr, H.F.J., F. Ferraccioli, N. Frearson, T. Jordan, C. Robinson, E. Armadillo, G. Caneva, E. Bozzo and I. Tabacco, 2007. Airborne  
274 Radio-Echo Sounding of the Wilkes Subglacial Basin, the Transantarctic Mountains, and the Dome C Region, Terra Antarctic Reports,  
275 **13**, 55–63.
- 276 Eisen, Olaf, 2008. Inference of velocity pattern from isochronous layers in firn, using an inverse method, Journal of Glaciology, **54**(187),  
277 613–630.
- 278 Fahnestock, M., W. Abdalati, S. Luo and S. Gogineni, 2001. Internal layer tracing and age-depth-accumulation relationships for the  
279 northern Greenland ice sheet, Journal of Geophysical Research, **106**(D24).
- 280 Ferraccioli, F., T. Jordan, E. Armadillo, E. Bozzo, H.F.J. Corr, G. Caneva, C. Robinson, N. Frearson and I. Tabacco, 2007. Collab-  
281 orative Aerogeophysical Campaign Targets the Wilkes Subglacial Basin, the Transantarctic Mountains and the Dome C Region,  
282 Terra Antarctic Reports, **13**, 1–36.
- 283 Hindmarsh, R.C.A., E.C. King, R. Mulvaney, H.F.J. Corr and F. Gillet-Chaulet, submitted. Ice flow at ice divide triple junctions II:  
284 observations from radar layer architecture, Journal of Geophysical Research.
- 285 Hindmarsh, R.C.A., G.J-M.C. Leysinger Vieli and F. Parrenin, 2009. A large-scale numerical model for computing isochrone geometry,  
286 Annals of Glaciology, **50**(51), 130–140.

- 287 IPCC, 2007. Climate Change 2007: The Physical Science Basis. Contribution of Working Group I to the Fourth Assessment Report of  
288 the Intergovernmental Panel on Climate Change [Solomon, S., D. Qin, M. Manning, Z. Chen, M. Marquis, K.B. Averyt, M. Tignor  
289 and H.L. Miller (eds.)], Tech. Rep. 4, Intergovernmental Panel on Climate Change, Cambridge University Press, Cambridge, United  
290 Kingdom and New York, USA.
- 291 Lemke, P., J. Ren, R.B. Alley, I. Allison, J. Carrasco, G. Flato, Y. Fujii, G. Kaser, P. Mote, R.H. Thomas and T. Zhang, 2007. Observations:  
292 Changes in Snow, Ice and Frozen Ground. Climate Change 2007: The Physical Science Basis. Contribution of Working Group I to  
293 the Fourth Assessment Report of the Intergovernmental Panel on Climate Change [Solomon, S., D. Qin, M. Manning, Z. Chen, M.  
294 Marquis, K.B. Averyt, M. Tignor and H.L. Miller (eds.)], (4).
- 295 Lythe, M., D. G. Vaughan and BEDMAP Consortium, 2001. BEDMAP: a new ice thickness and subglacial topographic model of  
296 Antarctica, Journal of Geophysical Research, **106**, 11335–11352.
- 297 Martín, C., G. H. Gudmundsson, H. D. Pritchard and O. Gagliardini, 2009. On the effects of anisotropic rheology on ice flow, internal  
298 structure, and the age-depth relationship at ice divides, Journal of Geophysical Research, **114**(F04001), doi:10.1029/2008JF001204.
- 299 Martín, C., R. C. A. Hindmarsh and F. J. Navarro, 2006. Dating ice flow change near the flow divide at Roosevelt Island,  
300 Antarctica, by using a thermomechanical model to predict radar stratigraphy, Journal of Geophysical Research, **111**(F01011),  
301 doi:10.1029/2005JF000326.
- 302 Matsuoka, K., A.G.H. Conway, G. Catania and C.F. Raymond, 2009. Radar signatures beneath a surface topographic lineation near the  
303 outlet of Kamb Ice Stream and Engelhardt Ice Ridge, West Antarctica, Annals of Glaciology, **50**(51), 98–104.
- 304 Nereson, N. A. and C. F. Raymond, 2001. The elevation history of ice streams and the spatial accumulation pattern along the Siple Coast  
305 of West Antarctica inferred from ground-based radar data from three inter-ice-stream ridges, Journal of Glaciology, 303–313.
- 306 Nereson, N. A., C. F. Raymond, R. W. Jacobel and E. D. Waddington, 2000. The accumulation pattern across Siple Dome, West  
307 Antarctica, inferred from radar-detected internal layers, Journal of Glaciology, 75–87.
- 308 Parrenin, F. and R. C. A. Hindmarsh, 2007. Influence of a non-uniform velocity field on isochrone geometry along a steady flowline of an  
309 ice sheet, Journal of Glaciology, **53**(183), 612–622.
- 310 Parrenin, F., R. C. A. Hindmarsh and F. Remy, 2006. Analytical solutions for the effect of topography, accumulation rate and lateral  
311 flow divergence on isochrone layer geometry, Journal of Glaciology, **52**(177), 191–202.
- 312 Rippin, D. M., M. J. Siegert, J. L. Bamber, D. G. Vaughan and H. F. J. Corr, 2006. Switch-off of a major enhanced ice flow unit in East  
313 Antarctica, Geophysical Research Letters, (15), doi:10.1029/2006GL026648.
- 314 Siegert, M.J., R.C.A. Hindmarsh and G.S Hamilton, 2003. Evidence for a large surface ablation zone in central East Antarctica during  
315 the last Ice Age, Quaternary Research, **59**(1), 114–121.
- 316 Siegert, M. J., B. Welch, D. Morse, A. Vieli, D. D. Blankenship, I. Joughin, E. C. King, G. J.-M. C. Vieli-Leysinger, A. J. Payne and  
317 R. Jacobel, 2004. Ice Flow Direction Change in Interior West Antarctica, Science, **305**(5692), 1948–1951.
- 318 Sime, L. C. and R. I. Ferguson, 2003. Information on Grain Sizes in Gravel-Bed Rivers by Automated Image Analysis,  
319 Journal of Sedimentary Research, **73**(4), 630–636.

320 Waddington, Edwin D., Thomas A. Neumann, Michelle R. Koutnik, Hans-Peter Marshall and David L. Morse, 2007. Inference of  
321 accumulation-rate patterns from deep layers in glaciers and ice sheets, International Glaciological Society, **53**(183), 694–712.

**Table 1.** Example RES dataset characteristics

	<b>F<sub>s</sub><sup>*</sup></b>	<b>EBW<sup>†</sup></b>	<b>CF<sup>‡</sup></b>
	<b>MHz</b>	<b>MHz</b>	<b>MHz</b>
Ground based (Fletcher)	100	5	7
Airborne (WSB)	22	5	150

\*Sampling frequency

†Effective band width

‡Centre Frequency

**Table 2.** Arrays generated and used during ARESP

<b>array</b>	<b>description</b>
$P$	initial RES echo strength dataset
$\overline{P_x}$	horizontal moving average of $P$ using length scale $L_x$
$\overline{P_{xz1}}$	vertical moving average of $\overline{P_x}$ using length scale $L_{z1}$ *
$\overline{P_{xz2}}$	vertical moving average of $\overline{P_x}$ using length scale $L_{z2}$ †
$B_1$	where $B_1 = \text{sign}(\overline{P_x} - \overline{P_{xz2}})$
$B_2$	where $B_1 = \text{sign}(\overline{P_{xz1}} - \overline{P_{xz2}})$

\*where  $L_{z1} = 0.5 \times \lambda$ †where  $L_{z2} = 2 \times \lambda$

**Table 3.** Properties of RES data and ARESP parameters

properties	description	value
$\Delta x_1$	horizontal pixel length	0.2 <i>m</i> for WSB only
$\Delta x_2$	horizontal pixel length	2 <i>m</i> for WSB and 2.73 <i>m</i> for Fletcher
$\Delta z$	vertical pixel length	0.0455 $\mu S$ or 3.8 <i>m</i> for WSB and 0.01 $\mu S$ or 0.84 <i>m</i> for Fletcher
$\lambda$	typical vertical layer wavelength	20 pixels or 76 <i>m</i> for WSB and 20 pixels or 16.8 <i>m</i> for Fletcher
averaging parameter	description	value
$L_x$	horizontal averaging length	500 pixels or 100 <i>m</i> , at $\Delta x_1 = 0.2 \text{ m}^*$
$L_{z1}$	intra layer vertical averaging length	$0.5 \times \lambda$ or 38 <i>m</i> for WSB and 8.4 <i>m</i> for Fletcher
$L_{z2}$	inter layer vertical averaging length	$2 \times \lambda$ or 152 <i>m</i> for WSB and 33.6 <i>m</i> for Fletcher
separation parameter	description	value
$S_1$	horizontal separation length for array $B_1$	50 pixels or about 25 <i>m</i> (or $2.5 \times \lambda$ in pixels) <sup>†</sup>
$S_2$	horizontal separation length for array $B_2$	100 pixels or about 50 <i>m</i> (or $5 \times \lambda$ in pixels)
object parameter	description	value
$A_1$	minimum area of retained 'layer object'	20 and 50 pixels for $B_1$ and $B_2$ , respectively
$A_2$	maximum area of retained 'layer object'	400 and 1000 pixels for $B_1$ and $B_2$ , respectively
$r$	minimum ratio of object length to height	3 in pixels <sup>‡</sup>

\*used for WSB only

<sup>†</sup>both WSB and Fletcher<sup>‡</sup>see  $\Delta x_2$  and  $\Delta z$ , above, for conversion to *m*

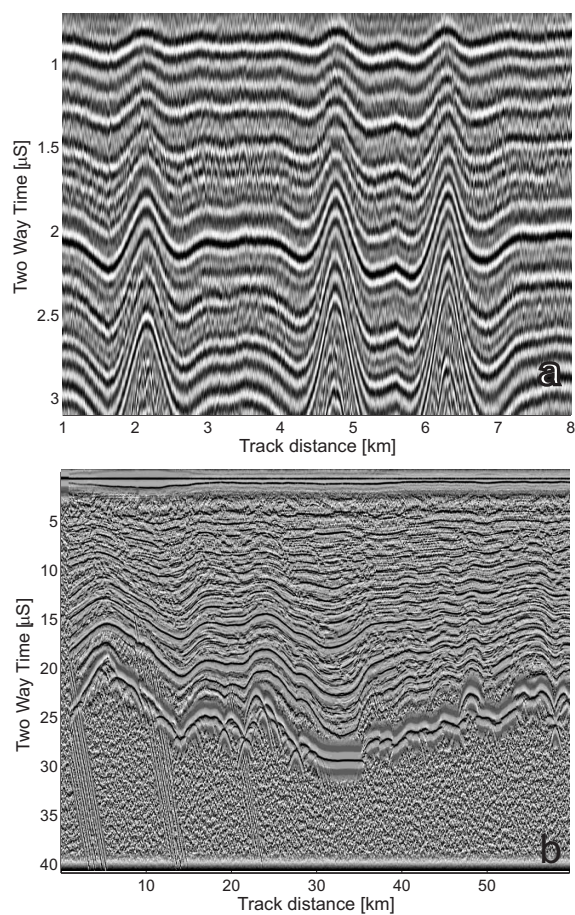


**Fig. 1.** Sample RES sections (a) 8 km of the ground-based Fletcher Promontory dataset, and (b) 59.63 km of the airborne WSB dataset. Both RES datasets are obtained along an approximately straight path. Layers are clarified by averaging adjacent traces and converting values to localised standard scores. The shading range for standard scores in each panel is  $\pm 2 \sigma$ .

## Schematic of radar processing method

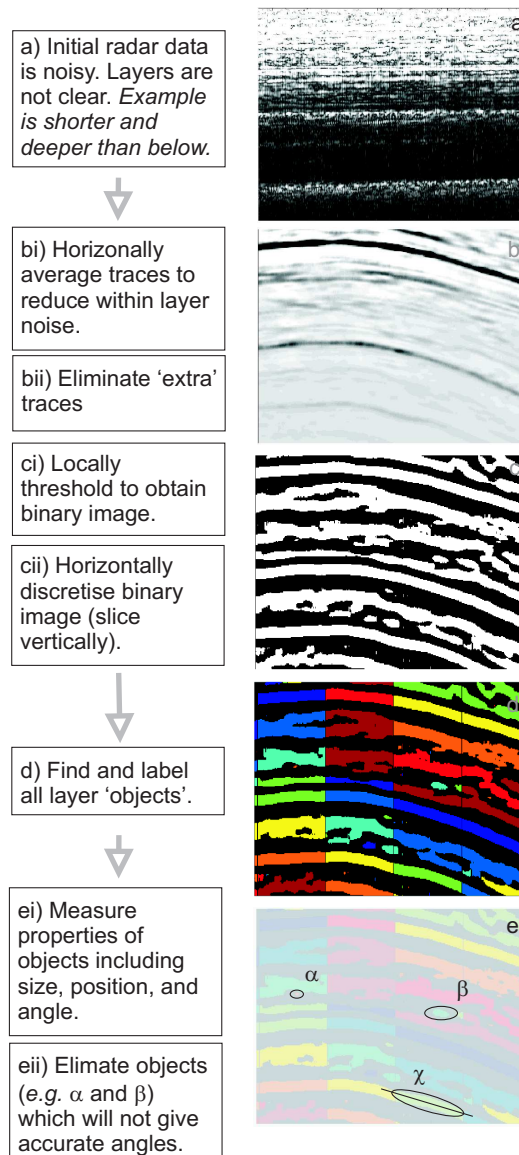


**Fig. 2.** Schematic description of processing method. Panels are illustrative, and are horizontally compressed to make the description clearer. a) Unprocessed data on a logarithmic grayscale. Note b) to e) show horizontally compressed data: (b) noise reduced data (logarithmic grayscale); (c) converted to binary; (d) horizontally sectioned with individual 'layer objects' coloured to indicate separate entities; (e) examples of 'layer objects' ( $\alpha$ ) and ( $\beta$ ) are too small and/or equi-axial so are excluded, whereas ( $\chi$ ) is a valid 'layer object'. Its orientation information is retained.

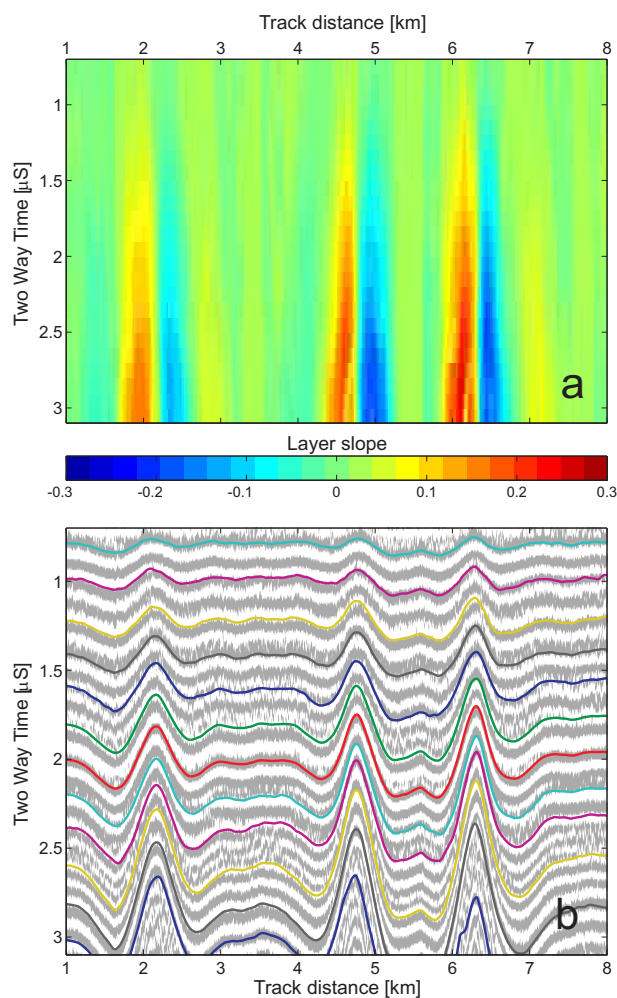


**Fig. 3.** Fletcher Promontory example ground based RES section. (a) The collated ARES layer slope data, and (b)  $B_2$  gray image overlaid with synthetic isochrone 'layers' projected from the layer dip data.

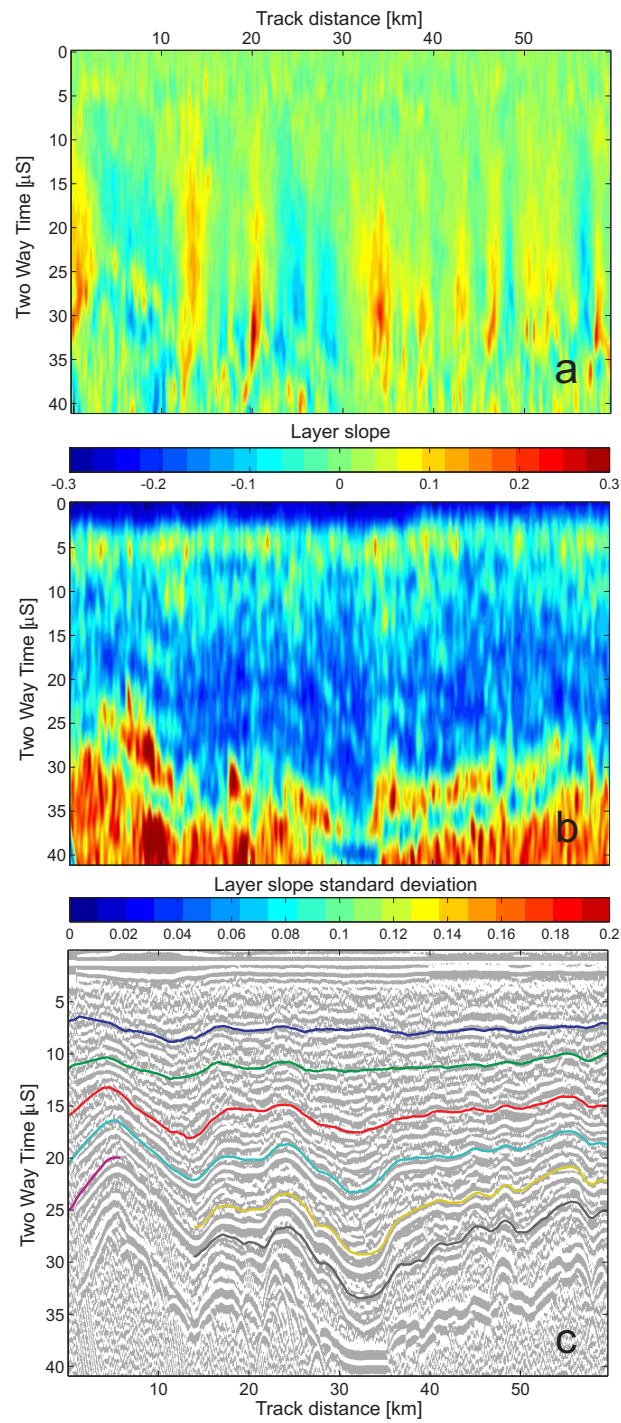


**Fig. 4.** WSB example airborne RES section. (a) Collated ARES layer slope data, (b) standard deviation associated with the ARES layer slope data, and (c) the WSB  $B_2$  gray image overlaid with synthetic isochrone 'layers' projected from the layer dip data.